Heterogeneous Tissue Modulus Improved Prediction of Mechanical Behavior in Osteoporotic Vertebral Cancellous Bone

Jason M. Cox[a], Joshua D. Smith[a], Marjolein C. H. van der Meulen[b], Jacqueline H. Cole[a]

[a]Joint Department of Biomedical Engineering, University of North Carolina, Chapel Hill, NC, and North Carolina State University, Raleigh, NC 27695, United States

[b]Meinig School of Biomedical Engineering, Cornell University, Ithaca, NY 14850, United States

J. M. Cox: jmcox9@ncsu.edu
J. D. Smith: jdsmit28@ncsu.edu
M. C. H. van der Meulen: mcv3@cornell.edu
*Corresponding Author, J. H. Cole: jacquecole@ncsu.edu

Abstract

The structural integrity of cancellous bone, which is essential to skeletal load-bearing capacity, is governed chiefly by apparent density, trabecular architecture, and tissue material properties. Metabolic bone disorders like osteoporosis can affect each of these factors separately, resulting in compromised load-bearing function. While the impact of apparent density and architecture on bone structural behavior has been well-documented, much less is known about the influence of tissue material properties, particularly in osteoporotic bone. The goal of this study was to isolate the influence of tissue material properties on normal and osteoporotic cancellous bone structural integrity, indicated by the apparent elastic modulus under uniaxial compression, using finite element (FE) models derived from 3D micro-computed tomography images. Three sets of models with increasing material detail were studied: 1) universal tissue elastic modulus, 2) specimen-specific average tissue modulus, and 3) heterogeneous tissue modulus. FE results were compared to matched parameters from physical testing. Increasing material detail did not significantly affect model predictions for normal bone. For osteoporotic bone, incorporating a specimen-specific tissue modulus significantly improved the ability of FE models to predict the apparent elastic modulus of physical specimens compared to using a universal tissue modulus. Incorporating material heterogeneity also improved model performance compared to models with a universal tissue modulus but did not afford significant improvement over models with specimen-specific average properties. We conclude that, while the influence of bone apparent density and trabecular architecture on structural integrity are dominant in healthy bone, average material properties also play a role in osteoporotic bone. Osteoporosis is diagnosed based primarily on apparent density, so these results highlight the need to consider other patient-specific differences that may affect average material properties, such as bone remodeling rate, in clinical assessments of osteoporotic bone structural integrity.

1. Introduction

The structural integrity of cancellous bone, which is essential to skeletal load-bearing capacity, is governed chiefly by apparent density, trabecular architecture, and tissue material properties (Beaupre and Hayes, 1985; Goldstein, 1987; Martin et al., 1998; Raux et al., 1975; Townsend et al., 1975). Although the impact of apparent density and architecture on bone structural behavior has been well-documented, much less is known about the influence of tissue material properties. Bone tissue is innately heterogeneous, exhibiting substantial spatial variation in tissue mineral content and quality (Bourne et al., 2002; Morgan et al., 2002; Paschalis et al., 1996, 1997a). Osteoporosis affects bone tissue properties, as generally evidenced by altered mineralization and changes in chemical composition (Gadeleta et al., 2000; Grynpas, 1993; Miller et al., 2000; Paschalis et al., 1997b). Changes in tissue properties may compromise the structural performance of bone, although the specific contributions of tissue mineralization and composition to bone mechanical properties have not been fully elucidated, particularly for cancellous bone.

Tissue properties are difficult to characterize experimentally and are primarily examined in small, excised bone volumes that likely do not fully capture the *in vivo* spatial variability. Computer models that simulate a virtual biopsy of cancellous bone can be used to investigate the mechanical behavior of a much larger region of bone and provide the opportunity to analyze that behavior noninvasively over changes in structural, material, and external loading parameters. Early finite element (FE) models treated cancellous bone as an irregular lattice-type structure and were used to assess the effect of idealized changes in architecture but not tissue properties (Beaupre and Hayes, 1985; Guo et al., 1994; Jensen et al., 1990; Silva and Gibson, 1997; Yeh and Keaveny, 1999). Architecture-based models, developed by converting voxels from a high-resolution micro-computed tomography (micro-CT) scan into cubic finite elements, more closely mimic the bone structure with fewer geometric assumptions than in the lattice models (Feldkamp et al., 1989). In the past, these voxel-based models were primarily used to examine the role of architecture in cancellous bone mechanical behavior through finite element analysis (FEA), and most assumed isotropic and homogeneous material properties (Hollister et al., 1994; Hou et al., 1998; Kabel et al., 1999a, 1999b; Ladd et al., 1998; Niebur et al., 2001, 2000; Ulrich et al., 1997; van Rietbergen et al., 1998, 1997, 1995). More recently, voxel-based modeling studies have investigated the interplay of cancellous bone mechanics and physiological processes such as microdamage progression (Liu et al., 2009), homeostatic bone remodeling (Hambli et al., 2011; McNamara and Prendergast, 2007), and bone remodeling following implantation of an orthopaedic device (Li et al., 2019; Schulte et al., 2013). Though these processes occur on a tissue-level scale where variable material properties may play a significant role, the assumption of material homogeneity is still common. Another recent approach to architecture-based FE modeling involves the use of beam elements to model whole trabeculae, dramatically reducing model degrees of freedom and therefore computational needs for FEA as well (van Lenthe et al., 2006; Wang et al., 2019). While this strategy is advantageous for analysis

throughput and produced accurate predictions of whole-bone level mechanical behavior, this approach prohibits the inclusion of physiological material heterogeneity and the investigation of tissue behavior at the sub-trabecular level.

Several studies have investigated the effects of incorporating tissue heterogeneity into FE models. Material heterogeneity in bone tissue manifests as variable tissue mineral density (ρ), which is initially low following surface-localized bone remodeling and increases through secondary mineralization as new bone tissue matures. Mineral density can be assigned to elements and converted to an elastic modulus (E), a parameter reflecting resistance to deformation, through empirically derived relationships. E-ρ relationships vary across species and bone sites (Beaupre and Hayes, 1985; Goulet et al., 1994; Helgason et al., 2008; Hodgskinson and Currey, 1992; Rice et al., 1988) but generally take a power law form (Currey, 1986). When cancellous bone tissue modulus was assigned this way, the variability negatively correlated with the apparent-level modulus of the whole bone and increased the percentage of failed tissue computed by comparing element strains to tissue yield strain (Jaasma et al., 2002). In another study, FE models that approximated realistic *in vivo* mineral distribution showed a decrease in apparent stiffness up to 4% when a linear E-ρ relationship was used and an increase up to 20% when a cubic relationship was used (van der Linden et al., 2001). However, these studies only examined a small volume of cancellous bone (4-5 mm cubic regions) for a small number of samples (n = 3), and the findings depended strongly on the assumed mineral distribution (Jaasma et al., 2002; van der Linden et al., 2001). For a given volume of cancellous bone, calibrated micro-CT scans provide an accurate representation of tissue mineral distribution (Homminga et al., 2001) that can be readily converted into a tissue modulus distribution through empirically derived E-ρ relationships. Studies utilizing this method have shown that incorporating heterogeneous tissue properties mimicking the *in vivo* distribution improved modulus prediction in rabbits (Bourne and van der Meulen, 2004) and humans (Knowles et al., 2019) but relied on less clinically relevant sites. Additionally, the study performed in rabbits concluded that specimen-specificity was more important than heterogeneity for improving predictions of apparent stiffness for specimens with low variability in tissue material properties.

Prior work suggests that controlled variability in bone tissue heterogeneity affects the mechanical properties predicted by finite element models. However, studies that extracted heterogeneous distributions from the samples themselves rather than imposing an assumed distribution do not show a conclusive effect in humans given their choice of a different species (Bourne and van der Meulen, 2004), a small sample size (Hammond et al., 2018; van Ruijven et al., 2007), an entirely male cohort (Renders et al., 2011, 2008), or a homogeneous control that did not match the average density of the heterogeneous test case (Knowles et al., 2019). Therefore, the question remains open as to whether physiological heterogeneity in FE models, and by extension *in vivo*, has a substantial influence on cancellous bone apparent properties. In addition, how the influence of heterogeneity depends on sex or the presence of metabolic bone disorders such as osteoporosis is not fully understood. Given that osteoporosis alters bone mineralization and the disparity in prevalence between sexes, these parameters need to be examined to test the robustness of these FE models. The objectives of this study were 1) to simulate the structural behavior of cancellous bone in the human spine using specimen-specific architecture- and material-based FE models, 2) to assess the effects of varied material models on the mechanical performance of the bone structure, 3) to compare model-derived parameters to experimentally measured mechanical properties of the cancellous specimens, and 4) to determine the effects of sex, bone site, and clinical bone status on the mechanical properties of the cancellous specimens across the various material models. Our approach was to model the architecture and material variations of human vertebral cancellous bone based on micro-CT scans, perform finite element analyses on the models, and compare the model predictions for different material distributions to experimentally measured mechanical properties of the same specimens.

2. Materials and Methods

2.1 *Subjects*

Cadaver spine segments were obtained from 19 Caucasian donors (10 female, 9 male) ages 58 to 92 years. For 18 donors, the spine segment extended from the 11th thoracic vertebra (T11) through the 4th lumbar vertebra (L4), and for one donor, the segment extended from T11 through the 2nd lumbar vertebra (L2). None of these spines showed evidence of vertebral fracture in a clinical bone density scan or of bone abnormalities during dissection, such as bone metastasis.

2.2 *Clinical Bone Density Scan*

Clinical bone mineral density status was assessed for all donors with dual-energy X-ray absorptiometry (DXA). Spine segments were secured in a curved Plexiglas® fixture, immersed in a saline bath within a Plexiglas® box, and scanned with a clinical fan-beam densitometer in lumbar spine array mode (Delphi QDR 4500A or QDR 4500W, Hologic Inc., Bedford, MA). T-score was computed for the L1-L4 subregion of each spine using the Hologic analysis software, and subjects were classified by T-score, according to the World Health Organization guidelines (Kanis et al., 1994), as Non-osteoporotic (T-score > -2.5) and Osteoporotic (T-score ≤ -2.5).

2.3 *Micro-Computed Tomography Scan*

To prepare small cancellous bone specimens for micro-CT, the T12 and L2 vertebrae were excised from each spine segment, and a full-depth cylindrical specimen (nominal diameter = 8.25 mm) was obtained from the center of each vertebra. The vertebra was secured in a drill press, and the cut was made along the superior-inferior axis at low speed under a continuous saline stream using a metal bond diamond core drill (Starlight Industries, Rosemont, PA). Cored specimens were wrapped in saline-soaked gauze and stored frozen at -20°C until scanning.

To obtain a voxel-based characterization of cancellous bone structure and mineralization, cored vertebral specimens were scanned using quantitative micro-CT (MS-8, GE Healthcare, London, Ontario, Canada) with 70 kVp X-ray tube peak potential, 90 µA X-ray intensity, and 3 s integration time. The specimens were scanned in saline treated with a protease inhibitor cocktail to minimize protein degradation in the bone tissue (P8340, Sigma-Aldrich Inc., St. Louis, MO) and then refrozen at -20°C until mechanical testing. The scans were reconstructed at an isotropic voxel size of 17.0 µm, and mineral density was calibrated using a phantom consisting of air, water, and a bone mineral standard (SB3, Gammex RMI, Middleton, WI) with a known density of 1.15 g/cc. For analysis, the scans were reoriented to align the superior-inferior axis of the core with the vertical axis in the manufacturer's software, and the ends of the cores were then cropped flat to a length of 17 mm (MicroView ABA 2.1.1., GE Healthcare, London, Ontario, Canada). Past work has suggested that the use of a global segmentation threshold for a cohort with a broad range of bone volume fraction or varying bone mineral density can result in an inaccurate topology (Bouxsein et al., 2010). To account for the inclusion of both osteoporotic and non-osteoporotic subjects in our cohort, specimen-specific thresholds were determined in the software using the Otsu method (N. Otsu, 1979). Bone volume fraction (BV/TV) and tissue mineral density (TMD) were assessed for each core.

2.4 *Mechanical Testing*

Following micro-CT scans, the cancellous bone cores were tested destructively in uniaxial compression, and apparent-level properties were assessed to validate the FE models. After the cortical end plates were removed, the bone core ends were glued inside snug-fitting brass caps using a previously documented protocol designed to minimize end artifacts (Keaveny et al., 1994). Approximately one-fourth of the overall core length was capped at each end. The diameter of each cancellous core was measured six times, and the exposed length was measured four times, using metric dial calipers, and the mean values were recorded. After the cyanoacrylate glue was cured for 24 hours at 4°C, the capped cores were preconditioned for 5 cycles between 0 and 0.10% compressive strain and then loaded monotonically to failure at a rate of 0.50% compressive strain per second (Mini-Bionix 858, MTS Systems Corporation, Eden Prairie, MN). Tests were conducted in displacement control at room temperature, and load and displacement data were sampled at 20 Hz. Displacement was measured with a 25-mm gage length axial extensometer (634.11F-24, MTS Systems Corporation, Eden Prairie, MN) attached to both brass caps. To compute apparent mechanical properties, load and displacement data were converted to apparent stress and strain using standard mechanics formulae (Hibbeler, 2000). The experimental apparent modulus was defined as the slope of a least-squares linear fit to the elastic region of the stress-strain data over 0.02-0.24% strain (Kopperdahl and Keaveny, 1998).

2.5 *Finite Element Modeling*

The micro-CT scans were used to build specimen-specific finite element (FE) models for all of the bone cores (Hollister et al., 1994; van Rietbergen et al., 1995). Using the thresholded micro-CT scans, bone voxels were converted into 8-node linear brick elements, creating a FE mesh measuring 8.25 mm in diameter and 17 mm in length (**Figure 1**). Elements unconnected to the primary structure were removed using the connectivity criterion of a 6-connected neighborhood. Unless an element shared a face with a portion of the primary bone structure, it was considered unconnected and was removed from the model. For all models, the number of unconnected elements removed was

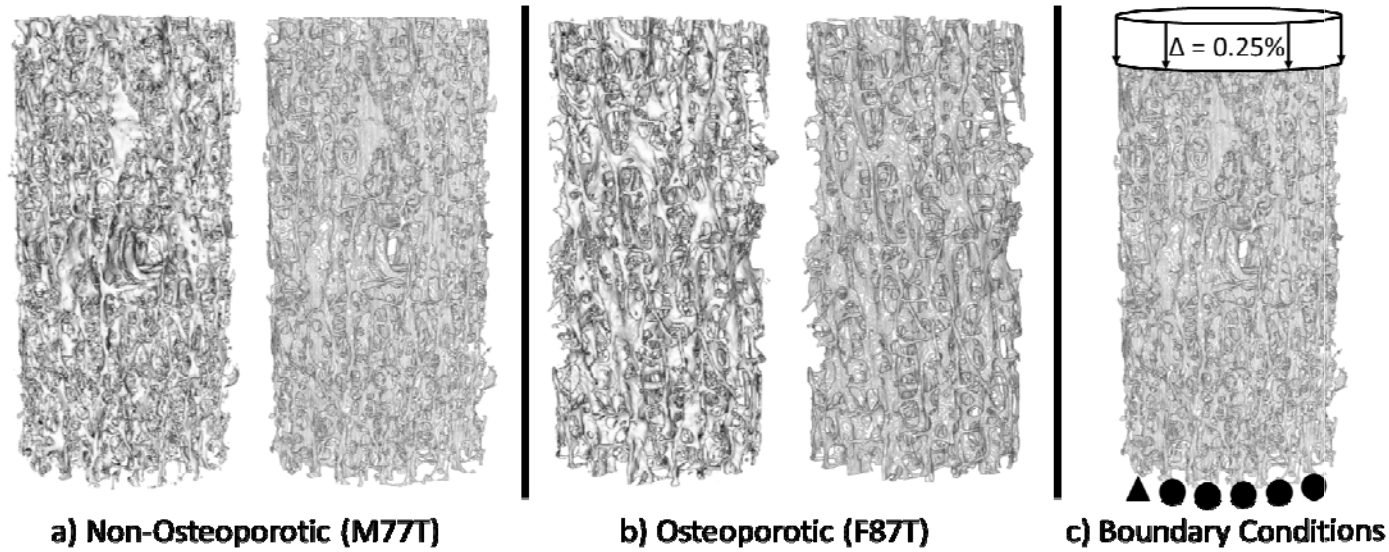

Figure 1: Examples of reconstructed volumes and finite element meshes for (a) non-osteoporotic and (b) osteoporotic subjects. Sex (M/F), age in years, and vertebral site (T=thoracic) are denoted. (c) Boundary conditions for finite element models. A compressive strain of 0.25% was applied to nodes on the top surface of the mesh. Nodes on the bottom surface were constrained to in-plane motion, except two adjacent nodes on the edge that were completely constrained to prevent rigid-body

between 0.6% and 7.6% of the total number of elements. On average, the final FE models had 24,000,000 elements and 33,000,000 nodes, for a total of 79,000,000 degrees of freedom.

Three sets of FE models were created for each bone core using different material properties. For each set, the models were assigned isotropic material properties with a constant Poisson's ratio of 0.3 and one of the following three tissue modulus distributions:

1. Universal Homogeneous (U_{hom}): A single homogeneous modulus of 20 GPa, chosen based on measurements from nanoindentation studies (Rho et al., 1999; Wang et al., 2006), was assigned to all elements for all bone core models.

2. Specimen-Specific Homogeneous (SS_{hom}): A unique homogeneous modulus was applied to all elements of each bone core model, computed using the mean voxel tissue density from micro-CT scans and a linear modulus-density relationship (Bourne and van der Meulen, 2004), as follows:

$$\frac{\quad}{\quad}$$

where E_c is the compressive tissue modulus for fully mineralized cortical bone (defined as 20 GPa), ρ_{mean} is the mean density over all mineralized voxels of the bone specimen, ρ_c is the density of the SB3 cortical bone mineral standard, and b is the exponent defining the nature of the E-ρ relationship (i.e., b = 1 for a linear relationship). Assuming a linear relationship between voxel tissue density and CT attenuation values, the ρ_{mean}/ρ_c ratio was computed using the ratio of the mean CT attenuation value to the SB3 mineral standard CT value.

3. Specimen-Specific Heterogeneous (SS_{het}): A unique heterogeneous modulus was computed for each element within each bone core model, using the same linear E-ρ formula, except ρ_{mean} was replaced by the individual voxel tissue density ρ_{voxel}, and E was computed individually for each element using the CT value for the associated voxel. Element moduli were then grouped into ~1,000 equally spaced bins to simplify material mapping while maintaining ample variability.

To account for scanning artifacts, which appear as abnormally high-density regions of the bone, ranges of measured tissue density for each model were computed and normalized to the value of ρ_c. These ranges were used to determine a global upper threshold of relative tissue density, and voxels with tissue densities above this threshold were assigned the

mean value of tissue densities computed from the remaining voxels. Less than 0.002% of elements in only three models were affected. Applying this correction prevented the rare scanning artifacts from artificially decreasing the degree of heterogeneity in the models by increasing the width of element modulus bins.

Boundary conditions were applied to the models to replicate displacement-controlled uniaxial compressive loading in the linear elastic range (**Figure 1c**). Pre-yield compression was simulated by displacing the nodes on the top surface of the cancellous core mesh to a strain of -0.25%. The nodes on the bottom surface of the mesh were treated as rollers constrained to in-plane motion only, and two adjacent nodes at one edge of the bottom surface were rigidly fixed to prevent rigid-body motion. The FE models were solved using a linear elastic static analysis (ABAQUS 6.3, HKS, Pawtucket, RI), and the model-predicted apparent modulus and distribution of minimum principal strains throughout the bone structure were obtained. The apparent modulus was calculated by summing the nodal reaction forces on the bottom surface of the core mesh and dividing by the cross-sectional area of a circle enclosing that surface. Additionally, the percent error in predicted apparent modulus relative to measured apparent modulus was computed. Minimum principal strain (ε_1) was analyzed at the element centroids throughout the model, and strain values were categorized as low (ε_1 < 500 microstrain), middle (500 microstrain ≤ ε_1 < 1500 microstrain), or high (ε_1 ≥ 1500 microstrain), and the proportions of elements belonging to each category (%Low, %Mid, %High) were determined. Because the distributions of ε_1 had a distinctly negative skew, with most of the values concentrated near zero, the median was used as the measure of centrality in lieu of the mean.

2.6 *Statistical Analyses*

All statistical models were constructed with SAS (SAS University Edition v. 9.4, SAS Institute Inc., Cary, NC) with a significance level of 0.05. Statistical models were used to determine the following: 1) effects of BV/TV, mean TMD, and TMD coefficient of variation (CV) on measured apparent modulus; 2) effects of apparent modulus estimation method (i.e., mechanical testing and three sets of models), sex, vertebral site, and osteoporosis status on apparent modulus; 3) effect of modulus estimation method on apparent modulus for subsets of the cohort separated by sex, site, and osteoporosis status; 4) effects of model material distribution, osteoporosis status, and their interaction on the absolute value of modulus prediction error; 5) effect of model material distribution and osteoporosis status on signed modulus prediction error as an indicator of error bias; 6) effect of osteoporosis status on signed prediction errors for each model material distribution; 7) the proportion of variance in the measured modulus explained by FE-predicted modulus alone and by FE-predicted modulus alongside osteoporosis status; 8) effects of model material distribution, sex, vertebral site, and osteoporosis status on ε_1; and 9) effect of model material distribution on ε_1 for subsets of the cohort separated by sex, site, and osteoporosis status.

Table 1: Mean tissue modulus (mod) for specimen-specific (SS) heterogeneous (het) and homogeneous (hom) models and mean apparent modulus calculated experimentally (exp) and for all models. Universal homogeneous (U_{hom}) models used a tissue modulus of 20 GPa.

Sex	Age	L1-L4 T-score	Bone Diagnosis	Bone Site	Tissue Mod (GPa) Mean (SD)	Mean Apparent Mod (GPa) E_{exp}	U_{hom}	SS_{hom}	SS_{het}
F	74	-0.8	Normal	Thoracic	20.6 (4.3)	0.51	0.55	0.56	0.56
				Lumbar	20.0 (4.5)	0.84	0.86	0.87	0.86
M	77	-0.8	Normal	Thoracic	20.2 (4.3)	0.62	0.62	0.63	0.62
				Lumbar	20.2 (4.5)	0.34	0.34	0.35	0.33
M	65	-1.2	Osteopenia	Thoracic	15.3 (4.2)	0.58	0.60	0.46	0.45
				Lumbar	15.2 (4.6)	0.55	0.67	0.51	0.50
M	79	-1.2	Osteopenia	Thoracic	21.2 (4.2)	0.63	0.64	0.68	0.67
				Lumbar	21.0 (4.3)	0.48	0.49	0.51	0.49
F	58	-1.5	Osteopenia	Thoracic	20.7 (4.4)	0.93	0.89	0.92	0.91
				Lumbar	21.9 (4.2)	0.73	0.62	0.67	0.67
M	71	-1.6	Osteopenia	Thoracic	20.3 (4.5)	0.56	0.64	0.65	0.65
				Lumbar	19.8 (4.9)	0.66	0.80	0.79	0.78
M	67	-1.7	Osteopenia	Thoracic	16.1 (4.4)	0.71	0.48	0.39	0.39
				Lumbar	15.9 (4.7)	0.48	0.69	0.55	0.54
M	63	-1.8	Osteopenia	Thoracic	19.1 (4.6)	0.39	0.48	0.45	0.44
				Lumbar	20.0 (4.5)	0.55	0.50	0.50	0.48
F	61	-1.9	Osteopenia	Thoracic	20.8 (4.7)	0.60	0.59	0.61	0.61
				Lumbar	19.0 (4.9)	0.59	0.55	0.52	0.51
M	63	-2.2	Osteopenia	Thoracic	21.9 (4.2)	0.70	0.66	0.73	0.73
				Lumbar	22.2 (4.1)	0.77	0.66	0.73	0.73
M	69	-2.3	Osteopenia	Thoracic	15.2 (5.3)	0.32	0.55	0.42	0.39
				Lumbar	15.5 (5.1)	0.35	0.45	0.35	0.34
F	92	-2.6	Osteoporosis	Thoracic	20.1 (4.3)	0.38	0.52	0.52	0.51
				Lumbar	19.6 (4.7)	0.47	0.48	0.47	0.46
M	64	-2.9	Osteoporosis	Thoracic	14.8 (4.6)	0.28	0.62	0.46	0.44
				Lumbar	18.4 (4.7)	0.60	0.72	0.67	0.64
F	61	-3.2	Osteoporosis	Thoracic	18.3 (4.9)	0.45	0.49	0.45	0.44
				Lumbar	19.7 (4.8)	0.45	0.44	0.43	0.42
F	87	-3.5	Osteoporosis	Thoracic	19.0 (4.7)	0.12	0.38	0.36	0.36
				Lumbar	19.5 (4.5)	0.43	0.38	0.37	0.37
F	87	-3.8	Osteoporosis	Thoracic	18.9 (4.7)	0.37	0.51	0.48	0.47
				Lumbar	19.9 (4.4)	0.40	0.34	0.34	0.33
F	68	-3.9	Osteoporosis	Thoracic	14.9 (4.7)	0.11	0.26	0.20	0.18
				Lumbar	14.5 (5.4)	0.17	0.52	0.38	0.37
F	65	-4.4	Osteoporosis	Thoracic	15.6 (4.6)	0.33	0.46	0.36	0.34
				Lumbar	15.3 (4.3)	0.29	0.36	0.27	0.26
F	79	-5.2	Osteoporosis	Thoracic	16.0 (5.8)	0.42	0.54	0.44	0.43
				Lumbar	15.9 (5.2)	0.20	0.29	0.23	0.23

Analysis #1. A preliminary mixed model

with BV/TV, mean TMD, and TMD CV as fixed effects revealed that TMD and TMD CV were highly correlated (r = -0.93). Therefore, a Gram-Schmidt orthonormal factorization of TMD CV was performed to isolate the orthogonal component relative to mean TMD, λ_{TMDCV}. A secondary model was then constructed with BV/TV, mean TMD, and λ_{TMDCV}.

Analysis #2. A mixed linear model was constructed with apparent modulus as the outcome variable. A preliminary model with full effects revealed that interactions between modulus estimation method, sex, vertebral site, and clinical bone status were not significant, so these interaction effects were not included in the final model to limit the number of comparisons. Analysis #3. Separate linear models for each subset were constructed, with apparent modulus as the outcome variable and modulus estimation method as the sole fixed effect.

Analysis #4. A mixed linear model was constructed with absolute modulus prediction error as the outcome variable. Fixed effects were limited to model material distribution, osteoporosis status and their interaction because initial results from analysis #1 indicated that sex and vertebral site had no significant influence on apparent modulus. Analysis #5. The mean signed modulus prediction error was compared to a hypothetical mean of 0 using one-sample t-tests for each combination of osteoporosis status and model material distribution. Analysis #6. Signed modulus prediction error for osteoporotic vs. non-osteoporotic models was compared for each material distribution using two-sample t-tests. Analysis #7. First, simple linear regression was performed to relate measured modulus to FE-predicted modulus for each modeled material distribution. Then, multiple linear regression was performed for each modeled material distribution by adding osteoporosis status as a second independent variable. The improvement in r^2 by adding osteoporosis status was calculated.

Analysis #8. Separate mixed linear models were constructed for median, standard deviation (SD), and %Low, %Mid, and %High λ_1 as the outcome variables. As with analysis #2, interaction effects were not included, as a preliminary model with full effects indicated they were not significant. Analysis #9. Separate linear models for each subset were constructed for median, SD, and %Low, %Mid and %High λ_1 as the outcome variables and model material distribution as the sole fixed effect.

To correct for each donor spine being represented twice in the dataset (for T12 and L2 vertebrae), donor ID was incorporated in all linear models as a random intercept effect. For each group of analyses outlined above, the Benjamini-Hochberg correction was applied to prevent multiple tests for effects from inflating the false discovery rate (Benjamini and Hochberg, 1995). In any model where modulus estimation method was identified as a significant variable, post hoc pairwise comparisons between methods were performed, and the Tukey-Kramer correction was applied.

3. Results

CT-based finite element models were developed for thoracic and lumbar vertebral cancellous bone cores of 19 subjects (10 female, 9 male), ages 58-92, with a broad range of DXA T-score (**Table 1**). Measured from micro-CT scans, bone volume fraction of the vertebral cores varied greatly, ranging from 5.8% to 14.1%, with a CV of 21%. Mean tissue mineral density from micro-CT varied slightly less, ranging from 0.56 to 0.85 g/cc, with a CV of 13%. The TMD distribution throughout the meshed bone volume, as assessed by normalized CT attenuation, varied somewhat across subjects, with CV ranging from 18.5% to 37.1%. Neither BV/TV, mean TMD, nor TMD CV differed significantly by subject sex, bone site, or clinical bone diagnosis (**Figure 2**). BV/TV and mean TMD were both positively associated with measured modulus ($p < 0.0001$ for both), whereas for a given value of mean TMD, TMD CV had only a marginal negative association with measured modulus ($p = 0.061$), as indicated by λ_{TMDCV}. For models with specimen-

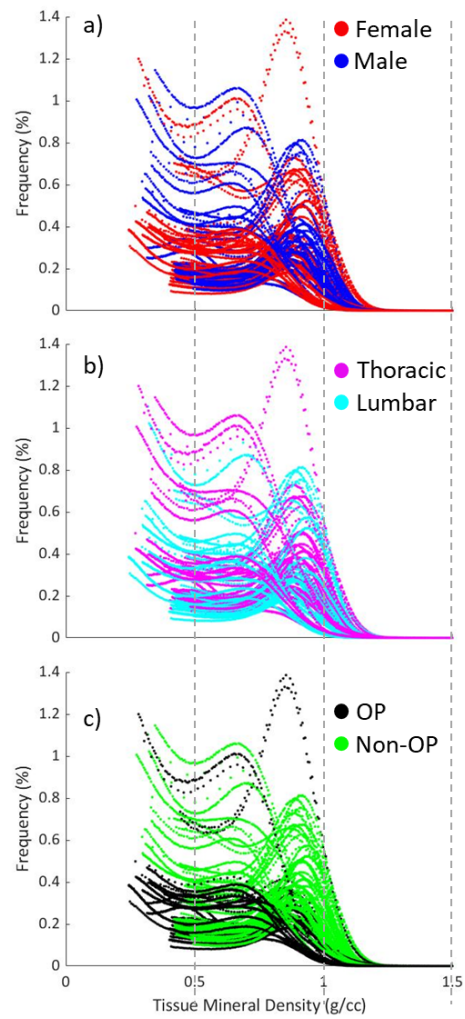

Figure 2: Bone tissue mineral density distribution assessed using CT attenuation for all 19 subjects, separated by (a) sex, (b) vertebral site and (c) clinical bone diagnosis (OP=osteoporotic). Shown are the percentages of voxels for each CT attenuation value, normalized by the CT value for the cortical bone phantom and scaled by its density (1.15 g/cc). The voxel densities shown here are only those above the bone threshold for each subject.

specific heterogeneous material properties, the distribution of bone tissue modulus was identical to that of tissue mineral density, given their linear relationship, and was similar in shape for all subjects. Overall, the heterogeneous tissue modulus averaged 14.5-22.2 GPa over all elements for a given model, resulting in a global mean of 18.5 GPa over all models (**Table 1**).

Under uniform compressive strain, predicted apparent modulus was similar across the three model sets, ranging 0.26-0.88 GPa for universal homogeneous models, 0.20-0.92 GPa for specimen-specific homogeneous models, and 0.18-0.91 GPa for specimen-specific heterogeneous models (**Table 1, Figure 3**). Overall, the FE models closely predicted experimentally measured apparent modulus, which ranged 0.11-0.93 GPa. Mean FE-predicted apparent modulus across all subjects was not significantly different from mean measured apparent modulus for any of the three assigned tissue modulus distributions ($p = 0.030$). Regardless of the estimation method, apparent modulus differed by clinical bone diagnosis, with 48% lower apparent modulus for osteoporotic compared to non-osteoporotic bone ($p = 0.009$, **Figure 3a**). Within the osteoporotic subset, universal homogeneous models had a significantly higher mean apparent modulus

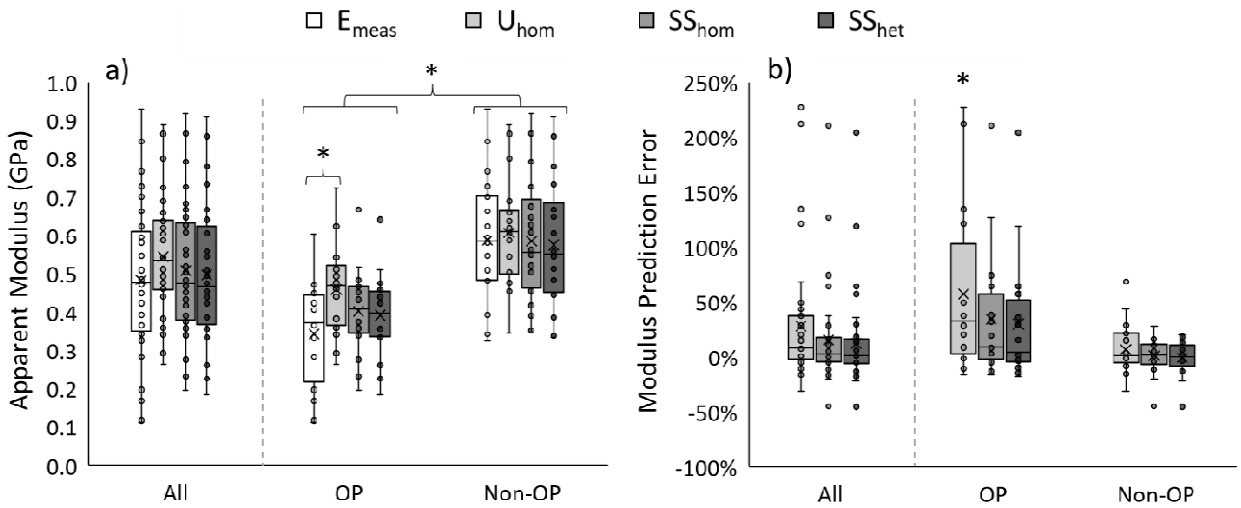

Figure 3: (a) Apparent modulus for each estimation method, shown for all subjects and subgroups by osteoporosis (OP) status. * $p < 0.05$. (b) Signed apparent modulus prediction error, shown for all subjects and subgroups by OP status, * $p < 0.05$ vs. mean of 0 and vs. non-OP.

compared to the mean experimentally measured modulus ($p = 0.046$, **Figure 3a**).

Across all subjects, the absolute value of apparent modulus prediction error between the FE-predicted and experimentally measured values did not differ by material distribution ($p = 0.88$, **Figure 3b**). Absolute apparent modulus prediction error trended 26% higher for osteoporotic models compared to non-osteoporotic models, but this effect was not quite significant after applying the Benjamini-Hochberg adjustment ($p = 0.061$). Additionally, osteoporosis status did not have a differential impact on apparent modulus prediction error among the three material distributions ($p = 0.68$). Signed apparent modulus prediction error was greater for osteoporotic compared to non-osteoporotic models by 57% for U_{hom} ($p = 0.034$, **Figure 3b**), but this difference was not significant for SS_{hom} ($p = 0.29$) or SS_{het} ($p = 0.29$). A significant bias toward overestimation of the measured modulus (prediction error > 0) was found only for U_{hom} osteoporotic models ($p = 0.0003$,

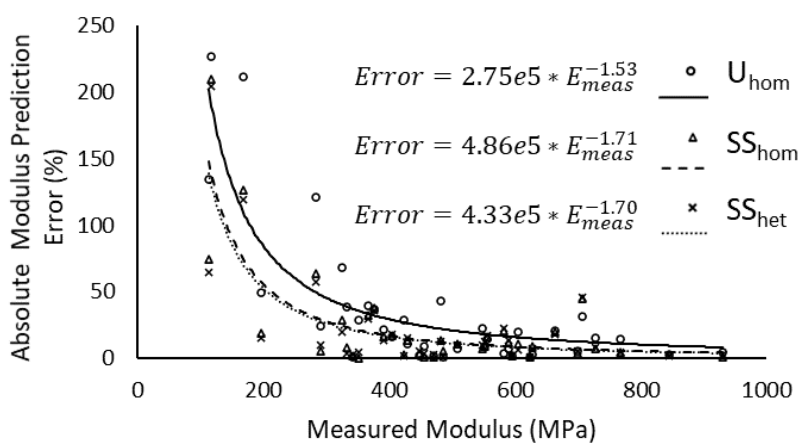

Figure 4: Absolute modulus prediction error for each model set, expressed as a percentage difference from the measured apparent modulus, E_{meas}. Data follow a negative power law trend.

Figure 3b). For each of the three model sets, apparent modulus prediction error decreased with increasing experimentally measured modulus, appearing to conform to a negative power law relationship (**Figure 4**).

Regardless of assigned modulus distribution, FE-predicted apparent modulus was linearly related to the experimental apparent modulus ($p < 0.0001$ for all cases) (**Figure 5a**). Overall, specimen-specific models predicted apparent modulus more reliably than universal homogeneous models ($r^2 = 0.61$ for U_{hom}, $r^2 = 0.74$ for SS_{hom}, and $r^2 = 0.75$ for SS_{het}). Among the categorical variables of sex, site, and clinical bone diagnosis, only clinical bone diagnosis had a significant effect on FE-predicted modulus. Incorporating clinical bone diagnosis improved the prediction of experimental apparent modulus by 8% for the universal model set and 4% for both specimen-specific model sets (**Figure 5b**).

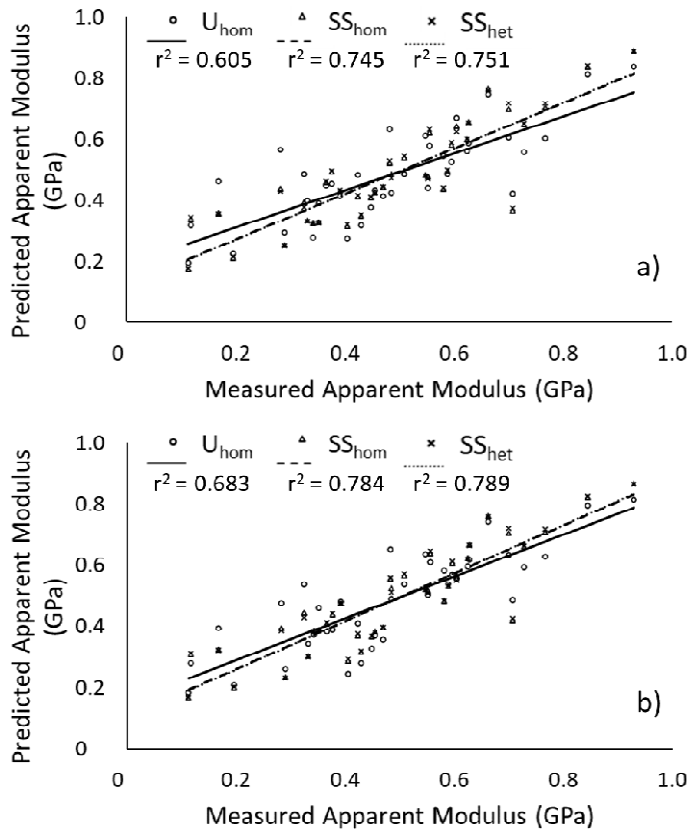

Figure 5: (a) FE-predicted apparent modulus for each model set was linearly related to measured apparent modulus. (b) Including clinical bone diagnosis as an explanatory variable improved r^2 for every model set, most prominently for U_{hom}.

Distributions of compressive minimum principal strain (ε_1) were evaluated throughout the model (**Figure 6**). Because FE analyses were linear and displacements were applied, the results for ε_1 were identical in both sets of homogeneous models (i.e., universal and specimen-specific). Therefore, only the results for universal homogeneous and specimen-specific heterogeneous models were evaluated. To avoid artificially high strains in elements near the applied load, a 14-mm central volume of interest was initially considered for analysis; because no significant difference in the proportion of high strain elements was found between a full-size volume and this central volume for either homogeneous ($p = 0.2$) or heterogeneous ($p=0.9$) models, all elements were included for strain analyses. For clarity, the values of compressive strain will be discussed in terms of the absolute value.

Distributions of ε_1 were similar for homogeneous and heterogeneous material models (**Figure 6**). Across all subjects only bone site had a significant effect on ε_1. Compared to T12 bone cores, L2 cores had a median ε_1 that was lower by 98 microstrain ($p < 0.0001$, **Figure 7a**), 3.8% more low-strain elements ($p = 0.0009$), and 3.6% fewer high-strain elements ($p < 0.0001$). When subjects were segmented by sex, bone site, and clinical bone diagnosis, the effect of model material distribution on ε_1 was only significant for L2 cores (**Figure 7a**). Within this subset, compared to heterogeneous models, homogeneous models displayed a higher median ε_1 by 92 microstrain ($p = 0.009$, **Figure 7a**), with 3.6% fewer low-strain elements ($p = 0.041$) and 3.0% more high-strain elements ($p = 0.009$) (**Figure 7b**).

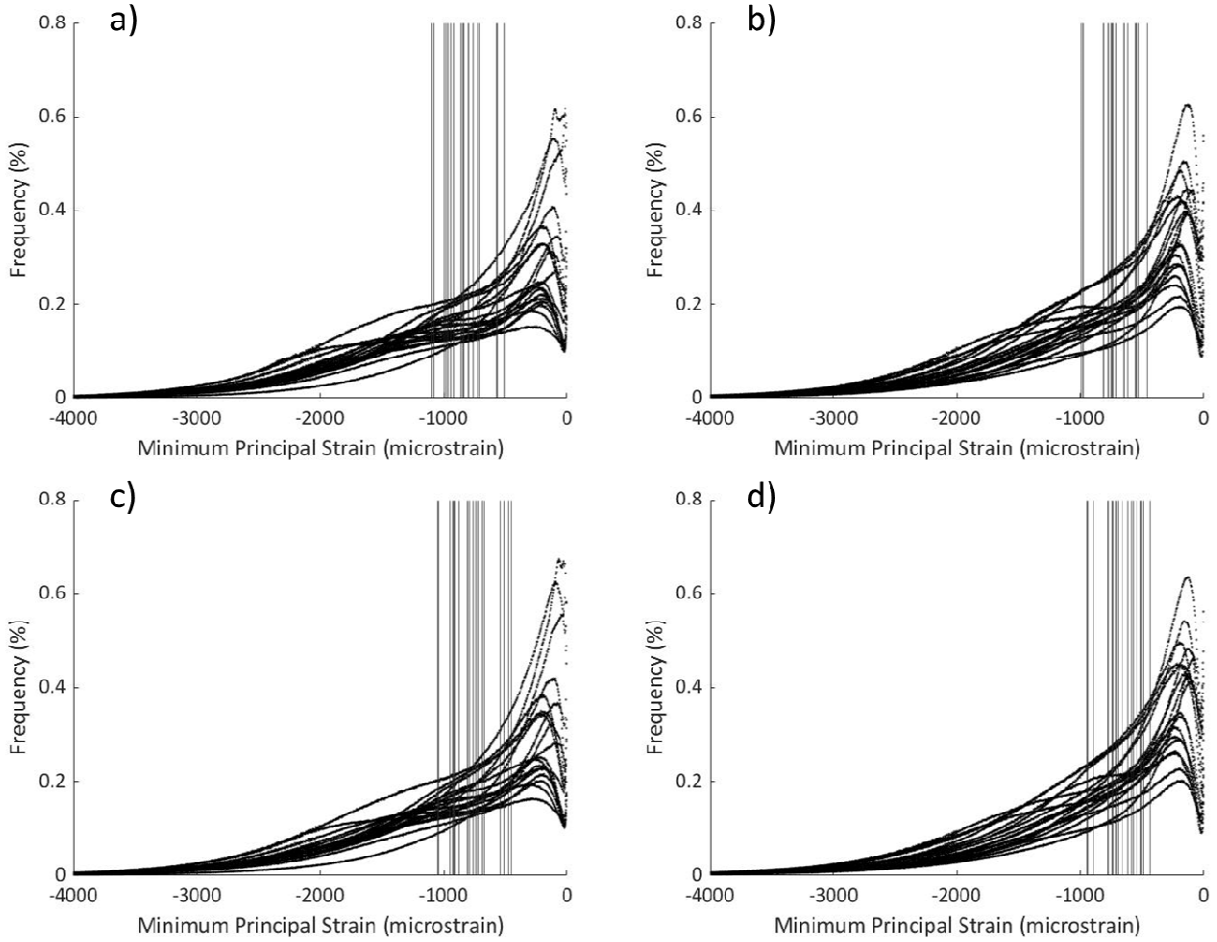

Figure 6: Distributions of tissue minimum principal strains (ε_1) throughout the entire bone volume for samples with universal homogeneous (a,b) and specimen-specific heterogeneous (c,d) material properties for all subjects, separated by T12 (a,c) and L2 bone sites (b,d). Vertical lines indicate the median value of ε_1 for each specimen.

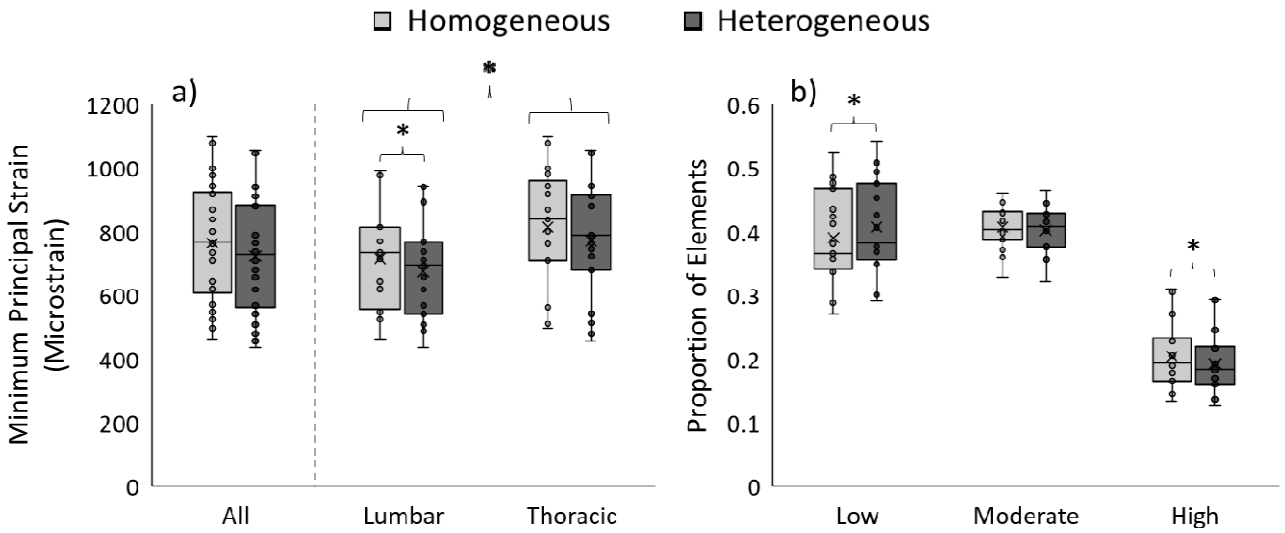

Figure 7: (a) Absolute value of the median minimum principal strain averaged over all subjects and subgroups by vertebral site. (b) Proportion of elements in each minimum principal strain group (Low, Middle, and High strain) for L2 bone cores. *$p < 0.05$.

4. Discussion

Material distributions derived from micro-CT for the specimen-specific heterogeneous models reflected true *in vivo* distributions over the volume of bone examined. For 24 out of 38 bone cores, the computed mean tissue modulus value was lower than the assumed value of 20 GPa for the U_{hom} group (**Table 1**), supporting the notion that the specimen-specific models may more accurately assess the structural competence of cancellous bone. Indeed, specimen-specific tissue moduli substantially improved the overall prediction of apparent modulus compared to models that assumed material homogeneity within and across subjects. By comparison, models incorporating intra-specimen material heterogeneity performed only marginally better than specimen-specific homogeneous models for predicting apparent elastic modulus. Similarly, while average TMD was strongly associated with apparent elastic modulus of physical bone cores, the degree of heterogeneity indicated by TMD variability was only marginally associated. The crucial factor in improving model performance - specimen-specificity or heterogeneity - is disputed (Bourne and van der Meulen, 2004; Hammond et al., 2018; Knowles et al., 2019; Renders et al., 2011, 2008; van Ruijven et al., 2007), although our results appear to support specimen-specificity for evaluating the elastic or linear response of bone under uniform compression. However, there were limitations to how heterogeneity was analyzed for both *ex vivo* and *in silico* testing.

For *ex vivo* testing, the limitation arises from the use of a single metric, TMD coefficient of variation, to represent heterogeneity. This metric alone does not explain differences in the *pattern* of the material heterogeneity between or within subjects. In general, trabecular bone tissue density is positively associated with distance from the trabecular surface and tissue age, owing to surface-localized bone remodeling that deposits low-density osteoid which then matures into denser bone tissue through secondary mineralization (Bourne and van der Meulen, 2004; Guo, 2001; Paschalis et al., 1997a). However, variations in bone remodeling rate or the rate of secondary mineralization may in turn create variability in the distribution of mineral density through the trabecular cross-section. The resulting influence on tissue mechanics can be illustrated by comparing a trabecula to a simple beam. For any bending beam, there is a gradient of strain magnitude that increases linearly from the beam central axis to the surface, running counter to the typical density gradient in a trabecula. Therefore, the specific distribution of mineral density may influence trabecular bending stiffness (van der Linden et al., 2001) in a manner that is not captured in a single metric such as TMD variability.

By comparison, our FE models allowed us to investigate the influence of material heterogeneity without relying on summary metrics but had other limitations such the assumption of purely elastic or linear element behavior. This assumption was a practical choice to greatly reduce the computational burden of FEA but prevented elements from exhibiting any plastic behavior (i.e., yielding). While the physical bone cores did behave elastically at the apparent-level up to and beyond 0.25% strain this does not guarantee that tissue-level behavior was purely elastic across all bone volumes. Some plastic behavior may have occurred in discrete locations of high strain, which as previously discussed may overlap with low-density bone tissue in bending trabeculae. Indeed, prior studies involving nonlinear FEA show a tendency for elements in transversely-oriented trabeculae to yield in tension, which suggests bending behavior given that the studied models underwent apparent-level compression (Liu et al., 2009; Torres et al., 2019). Plastic buckling in transverse trabeculae is thought to be a “sacrificial” behavior that dissipates the energy of extreme loads while keeping more structurally essential trabeculae intact (Hayes and Carter, 1976; Torres et al., 2019). However, these studies simulated either a much larger strain magnitude (Liu et al., 2009) or fatigue loading through multiple cycles (Torres et al., 2019). By comparison, our FE analyses did not involve extreme loads, so the effects of heterogeneity were not likely suppressed to a significant degree.

Aside from the limitations inherent in a linear, single step finite element analysis, our models assumed an isotropic stiffness for all elements despite *in vivo* bone tissue exhibiting material anisotropy, with greater yield strain and stiffness in compression than in tension. However, only an average of 0.04% of elements were in tension after uniform model compression, so this limitation likely had little impact on model performance. Additionally, our findings in high-resolution FE models are not directly translatable to models generated by clinical computed tomography. The voxel size of clinical CT images, approximately 61 µm for peripheral sites and 150 µm for spine, is considerably larger than the voxels used in this study. At clinical CT resolution, the sampling of bone material properties and architectural boundaries is subject to partial volume effects, which tend to lower the apparent modulus. This problem is exacerbated when modeling osteoporotic bone which has smaller architectural features due to trabecular thinning.

Despite the limitations of FEA, our investigation of strain distributions in lumbar models revealed that incorporating material heterogeneity did have a small effect at the tissue level. Homogeneous lumbar models had a higher median ε_1

than heterogeneous models as well as a higher apparent modulus. In other words, homogeneous models experienced slightly greater tissue deformation across the entire bone volume despite having a greater resistance to overall deformation. Additionally, for 17 out of 19 lumbar bone cores, heterogeneous models had a higher maximum ε_1. Though small, these differences suggest that material heterogeneity may facilitate strain concentration in small regions of the microstructure. This is consistent with hypothesis of sacrificial trabeculae raised by prior authors (Hayes and Carter, 1976; Liu et al., 2009; Torres et al., 2019; van der Linden et al., 2001), but the results of this study do not confirm that high strains were concentrated in bending transverse trabeculae, as would be expected. It is also unclear why only lumbar models displayed this behavior, but subtle differences in microarchitecture such as trabecular thickness, geometry, orientation, and their interaction may play a role. Further work exploring relationships between element strain, trabecular shape and orientation may elucidate the mechanisms by which material heterogeneity impacts cancellous bone mechanics at the level of individual trabeculae.

While previous studies have investigated the effect of varying material distributions in FE models (Bourne and van der Meulen, 2004; Jaasma et al., 2002; Renders et al., 2011, 2008; van der Linden et al., 2001; van Ruijven et al., 2007), the present study attempts to elucidate the role of material distribution in determining the mechanics of osteoporotic and healthy bone separately. Our results show that, among osteoporotic subjects, models that lack specimen-specificity tend to overestimate apparent stiffness in osteoporotic subjects. Models that only lack heterogeneity do not suffer the same downside. These findings offer additional support that specimen-specificity is more important for improving FE-based predictions of cancellous bone mechanical behavior than heterogeneity. Homogenization of material properties following osteoporosis has been reported (Vennin et al., 2017) and would explain the greater importance of average material properties versus heterogeneity. However, this is not borne out in our data as TMD variability was not significantly associated with clinical bone diagnosis.

Alternatively, our findings could be attributed to the strong negative correlation between average TMD and TMD CV in our subjects, which remained strong even when only osteoporotic subjects were considered ($r = -0.89$). Physiological processes such as bone remodeling offer a probable explanation for this relationship. For example, cancellous bone with many active remodeling sites may be more heterogeneous due to an increased abundance of osteoid, but by the same token will have lower average tissue density. As noted by prior authors, varying the degree of heterogeneity affects trabecular bending stiffness but *not* uniaxial compressive stiffness given a constant average density (Hayes and Carter, 1976). By comparison, varying average density affects both bending stiffness *and* uniaxial compressive stiffness for a trabecula. For vertebral bone under apparent compression, trabeculae aligned with the axis of loading are the main contributors to apparent modulus (Liu et al., 2006), and given their alignment it can be assumed that uniaxial stiffness of these trabeculae accounts for this contribution more so than bending stiffness. Therefore, since the applied load in our analyses matched the principal loading direction *in vivo* and lacked sufficient magnitude to generate substantial buckling in transverse trabeculae, it is reasonable that heterogeneity was less influential than average material properties for predicting apparent modulus, though heterogeneous models were still the best predictors overall.

Despite the importance of interactions between cancellous bone microarchitecture and material properties for mechanical behavior, they are not relevant to a diagnosis of osteoporosis, which is instead based solely on areal bone mineral density (aBMD) at a single timepoint. This issue is highlighted by previous work showing that aBMD alone does not fully explain the variability in bone strength among osteoporotic subjects (Greenspan et al., 1996; Moro et al., 1995; Perilli et al., 2012; Riggs et al., 1982; Schuit et al., 2004). Specimen-specific FE models of cancellous bone capture both microarchitecture and material properties in rich detail, and their interactions directly influence the outcome of FEA. While clinical imaging resolution is presently a barrier to the adoption of FE-based techniques, it will likely continue to improve. Additionally, further research to improve the performance of FE models may compensate for the drawbacks of lower resolution, accelerating their adoption into the clinic.

Among females, universal homogeneous models that overpredicted apparent modulus did so by an average of 62%, compared to 28% for males. Specimen-specific models that overpredicted apparent modulus did so by 46% for females and 16% for males. While specimen-specific finite element models predicted apparent stiffness similarly for males and females, adding tissue heterogeneity, whether within or between specimens, had a greater mean impact for females. For both males and females, specimen-specific heterogeneous and homogeneous FE models provided conservative estimates of tissue stiffness in all but one subject.

In the present study of vertebral bone specimens, the mean tissue elastic modulus for heterogeneous models (14.5-22.2 GPa) fell within the range of mean indentation modulus in human bone tissue examined by nanoindentation (7-32 GPa) (Donnelly et al., 2006; Rho et al., 1999; Wang et al., 2006; Zysset et al., 1999). The range of predicted apparent stiffness from our models (0.18-0.91 GPa) did not exceed the upper range computed in previous finite element studies of human cancellous bone (1.1 GPa), but did contain lower values than previously reported (0.42 GPa) (Hollister et al., 1994; van Lenthe et al., 2006; van Rietbergen et al., 1995). This is likely due to the substantial number of osteoporotic subjects in the present study, with experimentally measured apparent moduli as low as 0.11 GPa. Previous work investigating similar material property distributions in rabbit femora reported that specimen-specific model-predicted apparent moduli explained up to 9% more variation in experimentally measured moduli than universal models (Bourne and van der Meulen, 2004). By comparison, our specimen-specific models explained 10-15% more variation in experimentally measured moduli. The same study reported a 35% reduction in simulated apparent modulus by incorporating heterogeneous element material properties with a mean CV of 26%. Another study in human mandibular bone reported a 20% reduction in mean simulated apparent modulus by incorporating material heterogeneity (Renders et al., 2008). Our results showed a mere 2% reduction in simulated apparent modulus with the same mean CV in heterogeneous models. Both previous studies used small cancellous bone specimens (3-4 mm^3) which, along with differences in species and bone site, may account for this difference. In accordance with our results, another study conducted in mandibular bone showed a 2.5% decrease in mean element strain by incorporating material heterogeneity, although our results report a slightly greater decrease of 5.4%.

5. Conclusions

By comparing three sets of models of increasing complexity, we determined that the mean tissue modulus of vertebral cancellous bone is more important than tissue modulus heterogeneity for governing compressive elastic behavior. However, FE models that incorporate physiological material heterogeneity were the most accurate predictors of apparent modulus overall and were robust to differences in sex and clinical bone status. Heterogeneity may also be important for enabling certain FE models to replicate strain-concentrating adaptations of bone that protect it from damage under large apparent strain and may be more influential in nonlinear FEA aimed toward understanding the failure mechanisms of bone. Models that assume universal homogeneous material properties are particularly unsuited for predicting apparent modulus as they tend to overestimate osteoporotic bone stiffness. While these findings shed insight into the types of models that may prove useful for clinical bone evaluation in the future, the difference in imaging resolution between clinical CT and micro-CT remains a barrier, especially for osteoporotic bone. However, finite element models continue to excel at exploring the factors which govern bone mechanical behavior, a pursuit that foundationally rests on their accurate portrayal of mechanical properties. The findings presented here may help improve the accuracy of future FE-based research, particularly as it relates to osteoporotic bone.

6. References

Beaupre, G.S., Hayes, W.C., 1985. Finite element analysis of a three-dimensional open-celled model for trabecular bone. J. Biomech. Eng. 107, 249–256. https://doi.org/10.1115/1.3138550

Benjamini, Y., Hochberg, Y., 1995. Controlling the False Discovery Rate: A Practical and Powerful Approach to Multiple Testing. J. R. Stat. Soc. Ser. B Methodol. 57, 289–300.

Bourne, B., Morgan, T., Paschalis, E., van der Meulen, M., 2002. Cancellous bone anisotropy arises from both architecture and material properties, in: TRANSACTIONS OF THE ANNUAL MEETING-ORTHOPAEDIC RESEARCH SOCIETY. pp. 558–558.

Bourne, B.C., van der Meulen, M.C.H., 2004. Finite element models predict cancellous apparent modulus when tissue modulus is scaled from specimen CT-attenuation. J. Biomech. 37, 613–621. https://doi.org/10.1016/j.jbiomech.2003.10.002

Bouxsein, M.L., Boyd, S.K., Christiansen, B.A., Guldberg, R.E., Jepsen, K.J., Müller, R., 2010. Guidelines for assessment of bone microstructure in rodents using micro-computed tomography. J. Bone Miner. Res. Off. J. Am. Soc. Bone Miner. Res. 25, 1468–1486. https://doi.org/10.1002/jbmr.141

Currey, J.D., 1986. Power law models for the mechanical properties of cancellous bone. Eng. Med. 15, 153–154. https://doi.org/10.1243/emed_jour_1986_015_039_02

Donnelly, E., Williams, R.M., Downs, S.A., Dickinson, M.E., Baker, S.P., van der Meulen, M.C.H., 2006. Quasistatic and dynamic nanomechanical properties of cancellous bone tissue relate to collagen content and organization. J. Mater. Res. 21, 2106–2117. https://doi.org/10.1557/jmr.2006.0259

Feldkamp, L.A., Goldstein, S.A., Parfitt, A.M., Jesion, G., Kleerekoper, M., 1989. The direct examination of three-dimensional bone architecture in vitro by computed tomography. J. Bone Miner. Res. Off. J. Am. Soc. Bone Miner. Res. 4, 3–11. https://doi.org/10.1002/jbmr.5650040103

Gadeleta, S.J., Boskey, A.L., Paschalis, E., Carlson, C., Menschik, F., Baldini, T., Peterson, M., Rimnac, C.M., 2000. A physical, chemical, and mechanical study of lumbar vertebrae from normal, ovariectomized, and nandrolone decanoate-treated cynomolgus monkeys (Macaca fascicularis). Bone 27, 541–550. https://doi.org/10.1016/s8756-3282(00)00362-8

Goldstein, S.A., 1987. The mechanical properties of trabecular bone: dependence on anatomic location and function. J. Biomech. 20, 1055–1061. https://doi.org/10.1016/0021-9290(87)90023-6

Goulet, R.W., Goldstein, S.A., Ciarelli, M.J., Kuhn, J.L., Brown, M.B., Feldkamp, L.A., 1994. The relationship between the structural and orthogonal compressive properties of trabecular bone. J. Biomech. 27, 375–389. https://doi.org/10.1016/0021-9290(94)90014-0

Greenspan, S.L., Maitland-Ramsey, L., Myers, E., 1996. Classification of osteoporosis in the elderly is dependent on site-specific analysis. Calcif. Tissue Int. 58, 409–414. https://doi.org/10.1007/BF02509439

Grynpas, M., 1993. Age and disease-related changes in the mineral of bone. Calcif. Tissue Int. 53 Suppl 1, S57-64. https://doi.org/10.1007/BF01673403

Guo, X.E., 2001. Mechanical properties of cortical bone and cancellous bone tissue. Bone Mech. Handb. 10, 1–23.

Guo, X.E., McMahon, T.A., Keaveny, T.M., Hayes, W.C., Gibson, L.J., 1994. Finite element modeling of damage accumulation in trabecular bone under cyclic loading. J. Biomech. 27, 145–155. https://doi.org/10.1016/0021-9290(94)90203-8

Hambli, R., Katerchi, H., Benhamou, C.-L., 2011. Multiscale methodology for bone remodelling simulation using coupled finite element and neural network computation. Biomech. Model. Mechanobiol. 10, 133–145. https://doi.org/10.1007/s10237-010-0222-x

Hammond, M.A., Wallace, J.M., Allen, M.R., Siegmund, T., 2018. Incorporating tissue anisotropy and heterogeneity in finite element models of trabecular bone altered predicted local stress distributions. Biomech. Model. Mechanobiol. 17, 605–614. https://doi.org/10.1007/s10237-017-0981-8

Hayes, W.C., Carter, D.R., 1976. Postyield behavior of subchondral trabecular bone. J. Biomed. Mater. Res. 10, 537–544. https://doi.org/10.1002/jbm.820100409

Helgason, B., Perilli, E., Schileo, E., Taddei, F., Brynjólfsson, S., Viceconti, M., 2008. Mathematical relationships between bone density and mechanical properties: a literature review. Clin. Biomech. Bristol Avon 23, 135–146. https://doi.org/10.1016/j.clinbiomech.2007.08.024

Hibbeler, R.C., 2000. Mechanics of materials. Upper Saddle River, NJ: Prentice Hall; London: Prentice-Hall International (UK), [2000], Upper Saddle River, NJ.

Hodgskinson, R., Currey, J.D., 1992. Young's modulus, density and material properties in cancellous bone over a large density range. J. Mater. Sci. Mater. Med. 3, 377–381. https://doi.org/10.1007/BF00705371

Hollister, S.J., Brennan, J.M., Kikuchi, N., 1994. A homogenization sampling procedure for calculating trabecular bone effective stiffness and tissue level stress. J. Biomech. 27, 433–444. https://doi.org/10.1016/0021-9290(94)90019-1

Homminga, J., Huiskes, R., Van Rietbergen, B., Rüegsegger, P., Weinans, H., 2001. Introduction and evaluation of a gray-value voxel conversion technique. J. Biomech. 34, 513–517. https://doi.org/10.1016/s0021-9290(00)00227-x

Hou, F.J., Lang, S.M., Hoshaw, S.J., Reimann, D.A., Fyhrie, D.P., 1998. Human vertebral body apparent and hard tissue stiffness. J. Biomech. 31, 1009–1015. https://doi.org/10.1016/s0021-9290(98)00110-9

Jaasma, M.J., Bayraktar, H.H., Niebur, G.L., Keaveny, T.M., 2002. Biomechanical effects of intraspecimen variations in tissue modulus for trabecular bone. J. Biomech. 35, 237–246. https://doi.org/10.1016/s0021-9290(01)00193-2

Jensen, K.S., Mosekilde, L., Mosekilde, L., 1990. A model of vertebral trabecular bone architecture and its mechanical properties. Bone 11, 417–423. https://doi.org/10.1016/8756-3282(90)90137-n

Kabel, J., Odgaard, A., van Rietbergen, B., Huiskes, R., 1999a. Connectivity and the elastic properties of cancellous bone. Bone 24, 115–120. https://doi.org/10.1016/s8756-3282(98)00164-1

Kabel, J., van Rietbergen, B., Dalstra, M., Odgaard, A., Huiskes, R., 1999b. The role of an effective isotropic tissue modulus in the elastic properties of cancellous bone. J. Biomech. 32, 673–680. https://doi.org/10.1016/s0021-9290(99)00045-7

Kanis, J.A., Melton III, L.J., Christiansen, C., Johnston, C.C., Khaltaev, N., 1994. The diagnosis of osteoporosis. J. Bone Miner. Res. 9, 1137–1141. https://doi.org/10.1002/jbmr.5650090802

Keaveny, T.M., Guo, X.E., Wachtel, E.F., McMahon, T.A., Hayes, W.C., 1994. Trabecular bone exhibits fully linear elastic behavior and yields at low strains. J. Biomech. 27, 1127–1136. https://doi.org/10.1016/0021-9290(94)90053-1

Knowles, N.K., Ip, K., Ferreira, L.M., 2019. The Effect of Material Heterogeneity, Element Type, and Down-Sampling on Trabecular Stiffness in Micro Finite Element Models. Ann. Biomed. Eng. 47, 615–623. https://doi.org/10.1007/s10439-018-02152-6

Kopperdahl, D.L., Keaveny, T.M., 1998. Yield strain behavior of trabecular bone. J. Biomech. 31, 601–608. https://doi.org/10.1016/s0021-9290(98)00057-8

Ladd, A.J., Kinney, J.H., Haupt, D.L., Goldstein, S.A., 1998. Finite-element modeling of trabecular bone: comparison with mechanical testing and determination of tissue modulus. J. Orthop. Res. Off. Publ. Orthop. Res. Soc. 16, 622–628. https://doi.org/10.1002/jor.1100160516

Li, Z., Betts, D., Kuhn, G., Schirmer, M., Müller, R., Ruffoni, D., 2019. Mechanical regulation of bone formation and resorption around implants in a mouse model of osteopenic bone. J. R. Soc. Interface 16, 20180667. https://doi.org/10.1098/rsif.2018.0667

Liu, X.S., Bevill, G., Keaveny, T.M., Sajda, P., Guo, X.E., 2009. Micromechanical analyses of vertebral trabecular bone based on individual trabeculae segmentation of plates and rods. J. Biomech. 42, 249–256. https://doi.org/10.1016/j.jbiomech.2008.10.035

Liu, X.S., Sajda, P., Saha, P.K., Wehrli, F.W., Guo, X.E., 2006. Quantification of the roles of trabecular microarchitecture and trabecular type in determining the elastic modulus of human trabecular bone. J. Bone Miner. Res. Off. J. Am. Soc. Bone Miner. Res. 21, 1608–1617. https://doi.org/10.1359/jbmr.060716

Martin, R.B., 1940-, Burr, D.B., Sharkey, N.A., 1998. Skeletal tissue mechanics. New York: Springer, [1998], New York.

McNamara, L.M., Prendergast, P.J., 2007. Bone remodelling algorithms incorporating both strain and microdamage stimuli. J. Biomech. 40, 1381–1391. https://doi.org/10.1016/j.jbiomech.2006.05.007

Miller, L.M., Tibrewala, J., Carlson, C.S., 2000. Examination of bone chemical composition in osteoporosis using fluorescence-assisted synchrotron infrared microspectroscopy. Cell. Mol. Biol. Noisy--Gd. Fr. 46, 1035–1044.

Morgan, T.G., van der Meulen, M.C.H., Bourne, B.C., 2002. Density versus depth from trabecular surface measured by quantitative micro-CT, in: TRANSACTIONS OF THE ANNUAL MEETING-ORTHOPAEDIC RESEARCH SOCIETY. pp. 110–110.

Moro, M., Hecker, A.T., Bouxsein, M.L., Myers, E.R., 1995. Failure load of thoracic vertebrae correlates with lumbar bone mineral density measured by DXA. Calcif. Tissue Int. 56, 206–209. https://doi.org/10.1007/BF00298611

N. Otsu, 1979. A Threshold Selection Method from Gray-Level Histograms. IEEE Trans. Syst. Man Cybern. 9, 62–66. https://doi.org/10.1109/TSMC.1979.4310076

Niebur, G.L., Feldstein, M.J., Yuen, J.C., Chen, T.J., Keaveny, T.M., 2000. High-resolution finite element models with tissue strength asymmetry accurately predict failure of trabecular bone. J. Biomech. 33, 1575–1583. https://doi.org/10.1016/s0021-9290(00)00149-4

Niebur, G.L., Yuen, J.C., Burghardt, A.J., Keaveny, T.M., 2001. Sensitivity of damage predictions to tissue level yield properties and apparent loading conditions. J. Biomech. 34, 699–706. https://doi.org/10.1016/s0021-9290(01)00003-3

Paschalis, E.P., Betts, F., DiCarlo, E., Mendelsohn, R., Boskey, A.L., 1997a. FTIR microspectroscopic analysis of normal human cortical and trabecular bone. Calcif. Tissue Int. 61, 480–486. https://doi.org/10.1007/s002239900371

Paschalis, E.P., Betts, F., DiCarlo, E., Mendelsohn, R., Boskey, A.L., 1997b. FTIR microspectroscopic analysis of human iliac crest biopsies from untreated osteoporotic bone. Calcif. Tissue Int. 61, 487–492. https://doi.org/10.1007/s002239900372

Paschalis, E.P., DiCarlo, E., Betts, F., Sherman, P., Mendelsohn, R., Boskey, A.L., 1996. FTIR microspectroscopic analysis of human osteonal bone. Calcif. Tissue Int. 59, 480–487. https://doi.org/10.1007/BF00369214

Perilli, E., Briggs, A.M., Kantor, S., Codrington, J., Wark, J.D., Parkinson, I.H., Fazzalari, N.L., 2012. Failure strength of human vertebrae: prediction using bone mineral density measured by DXA and bone volume by micro-CT. Bone 50, 1416–1425. https://doi.org/10.1016/j.bone.2012.03.002

Raux, P., Townsend, P.R., Miegel, R., Rose, R.M., Radin, E.L., 1975. Trabecular architecture of the human patella. J. Biomech. 8, 1–7. https://doi.org/10.1016/0021-9290(75)90037-8

Renders, G. a. P., Mulder, L., Langenbach, G.E.J., van Ruijven, L.J., van Eijden, T.M.G.J., 2008. Biomechanical effect of mineral heterogeneity in trabecular bone. J. Biomech. 41, 2793–2798. https://doi.org/10.1016/j.jbiomech.2008.07.009

Renders, G. a. P., Mulder, L., van Ruijven, L.J., Langenbach, G.E.J., van Eijden, T.M.G.J., 2011. Mineral heterogeneity affects predictions of intratrabecular stress and strain. J. Biomech. 44, 402–407. https://doi.org/10.1016/j.jbiomech.2010.10.004

Rho, J.Y., Roy, M.E., Tsui, T.Y., Pharr, G.M., 1999. Elastic properties of microstructural components of human bone tissue as measured by nanoindentation. J. Biomed. Mater. Res. 45, 48–54. https://doi.org/10.1002/(sici)1097-4636(199904)45:1<48::aid-jbm7>3.0.co;2-5

Rice, J.C., Cowin, S.C., Bowman, J.A., 1988. On the dependence of the elasticity and strength of cancellous bone on apparent density. J. Biomech. 21, 155–168. https://doi.org/10.1016/0021-9290(88)90008-5

Riggs, B.L., Wahner, H.W., Seeman, E., Offord, K.P., Dunn, W.L., Mazess, R.B., Johnson, K.A., Melton, L.J., 1982. Changes in Bone Mineral Density of the Proximal Femur and Spine with Aging. J. Clin. Invest. 70, 716–723.

Schuit, S.C.E., van der Klift, M., Weel, A.E. a. M., de Laet, C.E.D.H., Burger, H., Seeman, E., Hofman, A., Uitterlinden, A.G., van Leeuwen, J.P.T.M., Pols, H. a. P., 2004. Fracture incidence and association with bone mineral density in elderly men and women: the Rotterdam Study. Bone 34, 195–202. https://doi.org/10.1016/j.bone.2003.10.001

Schulte, F.A., Ruffoni, D., Lambers, F.M., Christen, D., Webster, D.J., Kuhn, G., Müller, R., 2013. Local mechanical stimuli regulate bone formation and resorption in mice at the tissue level. PloS One 8, e62172. https://doi.org/10.1371/journal.pone.0062172

Silva, M.J., Gibson, L.J., 1997. Modeling the mechanical behavior of vertebral trabecular bone: effects of age-related changes in microstructure. Bone 21, 191–199. https://doi.org/10.1016/s8756-3282(97)00100-2

Torres, A.M., Trikanad, A.A., Aubin, C.A., Lambers, F.M., Luna, M., Rimnac, C.M., Zavattieri, P., Hernandez, C.J., 2019. Bone-inspired microarchitectures achieve enhanced fatigue life. Proc. Natl. Acad. Sci. U. S. A. 116, 24457–24462. https://doi.org/10.1073/pnas.1905814116

Townsend, P.R., Raux, P., Rose, R.M., Miegel, R.E., Radin, E.L., 1975. The distribution and anisotropy of the stiffness of cancellous bone in the human patella. J. Biomech. 8, 363–367. https://doi.org/10.1016/0021-9290(75)90071-8

Ulrich, D., Hildebrand, T., Van Rietbergen, B., Müller, R., Rüegsegger, P., 1997. The quality of trabecular bone evaluated with micro-computed tomography, FEA and mechanical testing. Stud. Health Technol. Inform. 40, 97–112.

van der Linden, J.C., Birkenhäger-Frenkel, D.H., Verhaar, J.A., Weinans, H., 2001. Trabecular bone's mechanical properties are affected by its non-uniform mineral distribution. J. Biomech. 34, 1573–1580. https://doi.org/10.1016/s0021-9290(01)00146-4

van Lenthe, G.H., Stauber, M., Müller, R., 2006. Specimen-specific beam models for fast and accurate prediction of human trabecular bone mechanical properties. Bone 39, 1182–1189. https://doi.org/10.1016/j.bone.2006.06.033

van Rietbergen, B., Majumdar, S., Pistoia, W., Newitt, D.C., Kothari, M., Laib, A., Rüegsegger, P., 1998. Assessment of cancellous bone mechanical properties from micro-FE models based on micro-CT, pQCT and MR images. Technol. Health Care Off. J. Eur. Soc. Eng. Med. 6, 413–420.

van Rietbergen, B., Weinans, H., Huiskes, R., 1997. Prospects of computer models for the prediction of osteoporotic bone fracture risk. Stud. Health Technol. Inform. 40, 25–32.

van Rietbergen, B., Weinans, H., Huiskes, R., Odgaard, A., 1995. A new method to determine trabecular bone elastic properties and loading using micromechanical finite-element models. J. Biomech. 28, 69–81. https://doi.org/10.1016/0021-9290(95)80008-5

van Ruijven, L.J., Mulder, L., van Eijden, T.M.G.J., 2007. Variations in mineralization affect the stress and strain distributions in cortical and trabecular bone. J. Biomech. 40, 1211–1218. https://doi.org/10.1016/j.jbiomech.2006.06.004

Vennin, S., Desyatova, A., Turner, J.A., Watson, P.A., Lappe, J.M., Recker, R.R., Akhter, M.P., 2017. Intrinsic material property differences in bone tissue from patients suffering low-trauma osteoporotic fractures, compared to matched non-fracturing women. Bone 97, 233–242. https://doi.org/10.1016/j.bone.2017.01.031

Wang, J., Zhou, B., Hu, Y., Zhang, Z., Yu, Y.E., Nawathe, S., Nishiyama, K.K., Keaveny, T.M., Shane, E., Guo, X.E., 2019. Accurate and Efficient Plate and Rod Micro Finite Element Whole Bone Models Based on High-Resolution Peripheral Computed Tomography. J. Biomech. Eng. https://doi.org/10.1115/1.4042680

Wang, X., Chen, X., Hodgson, P., Wen, C., 2006. Elastic modulus and hardness of cortical and trabecular bovine bone measured by nanoindentation. Trans. Nonferrous Met. Soc. China 16, s744–s748. https://doi.org/10.1016/S1003-6326(06)60293-8

Yeh, O.C., Keaveny, T.M., 1999. Biomechanical effects of intraspecimen variations in trabecular architecture: a three-dimensional finite element study. Bone 25, 223–228. https://doi.org/10.1016/s8756-3282(99)00092-7

Zysset, P.K., Guo, X.E., Hoffler, C.E., Moore, K.E., Goldstein, S.A., 1999. Elastic modulus and hardness of cortical and trabecular bone lamellae measured by nanoindentation in the human femur. J. Biomech. 32, 1005–1012. https://doi.org/10.1016/s0021-9290(99)00111-6